Regenerative Medicine and Dentistry
https://www.sciltp.com/journals/rmd

Article

Substrate-Independent Antibacterial Coatings with Optimal Concentration of Covalently Immobilised Silver Nanoparticles That Support Osteogenesis

Neethu Ninan [1,2], Fei Wei [3], Dennis Palms [1], Peter Zilm [4], Yunpeng Zhao [5], Richard Bright [1,*], Yin Xiao [3,6,7] and Krasimir Vasilev [1,*]

[1] College of Medicine and Public Health, Flinders University, Bedford Park, Adelaide, SA 5042, Australia
[2] Academic Unit of STEM, University of South Australia, Mawson Lakes, Adelaide, SA 5095, Australia
[3] The Australia-China Centre for Tissue Engineering and Regenerative Medicine, Queensland University of Technology, Brisbane, QLD 4059, Australia
[4] Translational Research in Oral Health Science, Adelaide Dental School, The University of Adelaide, Adelaide, SA 5005, Australia
[5] Department of Orthopedics, Qilu Hospital of Shandong University, Jinan 250012, China
[6] School of Medicine and Dentistry, Griffith University, Gold Coast Campus, Southport, QLD 4222, Australia
[7] Institute for Biomedicine and Glycomics, Griffith University, Southport, QLD 4222, Australia
* Correspondence: richard.bright@flinders.edu.au (R.B.); krasimir.vasilev@flinders.edu.au (K.V.)

How To Cite: Ninan, N.; Wei, F.; Palms, D.; et al. Substrate-Independent Antibacterial Coatings with Optimal Concentration of Covalently Immobilised Silver Nanoparticles That Support Osteogenesis. *Regenerative Medicine and Dentistry* **2025**, *2*(3), 11. https://doi.org/10.53941/rmd.2025.100011

Received: 12 August 2025
Revised: 2 September 2025
Accepted: 4 September 2025
Published: 10 September 2025

Abstract: Medical device-associated infections remain a major clinical challenge, frequently leading to implant failure, patient morbidity and mortality, and high healthcare costs. Equally critical is effective device osteointegration, which is often compromised in environments prone to infection. Here, we present a multifunctional, substrate-independent surface coating that simultaneously imparts robust antibacterial activity and promotes osteogenesis through modulation of inflammation. A thin plasma polymer layer derived from 2-methyl-2-oxazoline was deposited on material substrates to facilitate covalent binding of controlled concentrations of silver nanoparticles (AgNPs), functionalized with 2-mercaptosuccinic acid using oxazoline ring-opening chemistry. The coatings exhibited potent antibacterial effects against both Gram-positive and Gram-negative pathogens, including *Staphylococcus aureus*, *Staphylococcus epidermidis*, *Escherichia coli*, and *Pseudomonas aeruginosa*, while maintaining cytocompatibility with human cells. Mechanistic studies revealed that the AgNPs functionalized surfaces exhibited a concentration-dependent modulation of inflammatory cytokine and osteoclastogenic markers expression in macrophages, while promoting osteogenic signalling in co-cultured human bone marrow stromal cells. Coatings having immobilized AgNP at a concentration of 9 At% achieved an optimal balance between antibacterial efficacy and osteoimmunomodulation. This study demonstrates that finely tuning the AgNPs surface concentration can deliver a bioactive coating platform with dual antibacterial and osteogenic functionality, offering promising translational potential for a wide range of medical implants where osteointegration is vital, such as in orthopaedics and dentistry.

Keywords: plasma polymerization; antibacterial; osteogenesis; silver nanoparticle; surface functionalization; implant infection

1. Introduction

Infected medical devices are responsible for more than 50% of all hospital-acquired infections, posing a serious risk to patient health and significantly burdening healthcare systems [1–3]. Over one million infections occur annually in the United States alone, with treatment costs ranging from $30,000 to $300,000 per case [4–6]. Similar challenges are observed globally, including in dialysis patients, where infection-related mortality remains high [7]. The burden is even greater in resource-limited settings due to inadequate sanitation and poor hygiene conditions [8–10].

Many regard antibiotics as one of the most significant medical discoveries of the 20th century, having saved countless lives over the past 70 years [11,12]. However, treatment is often delayed until biofilms have formed, making bacteria up to 1000 times more resistant to antibiotics [13,14]. Consequently, much higher doses are needed for treatment, increasing the risk of systemic toxicity to organs such as the liver and kidneys [15,16]. Biofilms protect bacteria from the host immune system and facilitate gene exchange, contributing to the rise of antibiotic resistance, a growing challenge in infection treatment [17]. In recent decades, the rise of antibiotic-resistant infections has posed a significant challenge to effective treatment [12,18,19].

The difficulties presented by medical device-related infections, along with the understanding that they all begin with the attachment of individual bacterial cells to the device surface, have given rise to the concept of antibacterial coatings. Hypothetically, if the initial bacterial attachment to solid surfaces can be prevented, biofilm would not form, which could significantly improve the outcomes of medical procedures. This concept has inspired intense research and development activities in academia and the biomedical industry. Numerous antibacterial coating platforms have been developed and are reviewed extensively elsewhere [20–24].

One well-recognized opportunity is the use of surface coatings that utilize silver, silver-based compounds, and silver nanoparticles as antibacterial agents [25,26]. Silver has been used in medical treatments for millennia and its benefits to wound healing were documented in antiquity [27]. At least two reasons caused the resurgent interest in silver: (i) the increasing prevalence of antibiotic-resistant bacteria and (ii) the existence of pathogens that antibiotics cannot kill. Today, many medical devices, such as catheters [28] and dressings [29,30], utilize silver coatings. Despite some controversy, its medical use is growing, driving continued efforts to improve surface delivery.

Despite considerable progress in antibacterial coatings, most existing technologies, while capable of inhibiting bacterial attachment to different degrees, may cause host cell and tissue toxicity. The latter is vitally important when it comes to medical devices. Thus, there is a critical need for multifunctional coatings that not only prevent infection but also stimulate tissue regeneration.

Recently, we have developed plasma polymer coatings deposited from oxazoline precursors (POX) [31,32]. One valuable property of these coatings is their ability to inhibit biofilm formation [33]. Together with other beneficial properties, such as excellent biocompatibility and a reduction in inflammatory marker expression, these coatings are excellent candidates for placement on medical device surfaces. [31,32] The substrate-independent nature of the technique for deposition means that coatings can be deposited on any material surface, which offers a technological advantage [34,35]. In comparison, other methods for surface modification, such as layer-by-layer assembly or self-assembled monolayers, require a specific substrate, which makes it challenging to transfer the same coating to different medical devices [36]. Importantly, POX coatings uniquely retain oxazoline functionalities, facilitating the covalent binding of carboxylic acid functional ligands and nanoparticles [32,37,38].

The hypothesis underpinning this study is that fine-tuning the concentration of silver nanoparticles on the surface of the biomaterial can achieve both antibacterial properties and stimulate tissue regeneration. This hypothesis is substantiated by several prior studies by our team, which show that the concentration of released silver ions is key to achieving potent activity against bacteria and preventing cytotoxicity [39–41]. To achieve the desired dual-function substrate-independent coatings, we used plasma polymers derived from oxazoline precursors and covalently immobilized silver nanoparticles (AgNPs@MSA) in two different surface concentrations. The antibacterial efficacy was tested against clinically relevant pathogens, including *Staphylococcus aureus*, *Staphylococcus epidermidis, Escherichia coli*, and *Pseudomonas aeruginosa*. We also mechanistically evaluated the biocompatibility, immunomodulatory and osteogenic properties of the coatings in specifically designed in vitro models.

2. Materials and Methods

2.1. Materials

2-mercaptosuccinic acid (MSA, 97%), NaOH pellets, silver nitrate ($AgNO_3$), 2-methyl-2-oxazoline, nitric acid (70%), sodium borohydride ($NaBH_4$), phosphate-buffered saline (PBS), and acetic acid (33%) were purchased from Sigma Aldrich (Burlington, MA, USA). Hydrochloric acid (36%) and safranin were bought from Ajax

Finechem Pty Ltd., Australia. Dulbecco's Modified Eagle Medium, fetal bovine serum (FBS), 4% formaldehyde, penicillin (100 IU mL^{-1}), streptomycin (100 mg mL^{-1}), TRIzol reagent were purchased from Gibco, Life Technologies (Carlsbad, CA, USA). Glass slides, glass coverslips, carbon-coated copper grids and Thermanox coverslips were bought from Pro Sci-Tech, Qld, Australia. Nutrient agar and Tryptone soy broth (TSB) were purchased from Oxoid. Alexa Fluor® 488 Conjugate anti-rabbit IgG secondary antibody was procured from Cell Signaling Technology. Ultra-pure Milli-Q water was used for all experiments and cleaning procedures. cDNA Synthesis Kit was procured from Bioline NSW, Australia, and the ELISA kit for immune studies was purchased from R&D Systems, MN, USA. 6-well transwell inserts with a pore size of 0.4 μm were purchased from Becton-Dickinson Labware (Franklin Lakes, NJ, USA).

2.2. Plasma Deposition

Plasma deposition was carried out in a custom-built bell-chamber reactor capable of capacitive coupling, with a plasma generator functioning at 13.56 MHz and a related network (Advanced Energy, Denver, CO, USA) [42]. First, silicon wafers, glass slides, and Thermanox coverslips were cleaned with acetone and ethanol, dried with a nitrogen stream, and subsequently vacuum-sealed for further use. Before any plasma deposition, the substrates were cleaned using air plasma (50 W, 5 min, 1×10^{-1} mbar) to remove undesired organic contaminants. Plasma polymer films of 2-methyl-2-oxazoline were deposited for 2 min at a monomer pressure of 2×10^{-1} mbar at 50 W. To stabilize the plasma coating, the substrates were vacuum-sealed and kept overnight at room temperature before further modification.

2.3. Synthesis of AgNPs@MSA and Subsequent Immobilization

AgNPs@MSA were synthesized by reducing $AgNO_3$ with $NaBH_4$, as previously reported [43]. Briefly, 5 mL of MSA (2 mM) was added to 12 mL of $AgNO_3$ (2 mM) in the presence of ice cubes. Next, 0.5 mL of $NaBH_4$ (0.5 M) was added dropwise to the solution under vigorous stirring. The color of the solution mixture changed from colorless to reddish-brown after the addition of $NaBH_4$, indicating the formation of nanoparticles. The AgNPs@MSA were stored at 4 °C in dark conditions, and the solutions remained stable for six months without any precipitation. The AgNPs@MSA immobilization on the POX substrates was achieved by directly immersing the modified substrates in the nanoparticle solution at room temperature for 6 h and 24 h. After incubation, the AgNPs@MSA solution was removed, and the samples were washed three times with Milli-Q water to remove any unbound AgNPs@MSA. The samples were then dried with a nitrogen stream and vacuum sealed until further use. Herein, POX refers to polyoxazoline-coated samples. Ag-6h and Ag-24h are polyoxazoline-coated samples immobilized with AgNPs@MSA for 6 h and 24 h, respectively.

2.4. Transmission Electron Microscope (TEM)

The morphological and structural properties of POX, Ag-6h and Ag-24h surfaces were characterized using a JEOL-2100F TEM (JEOL Ltd., Tokyo, Japan), operated at an accelerating voltage of 200 kV. To prepare samples for TEM analysis, a freshly prepared nanoparticle suspension was subjected to thorough ultrasonication to ensure a uniform dispersion and to minimize agglomeration. Subsequently, 5 μL of the sonicated suspension was carefully dropped onto a carbon-coated copper grid (300 mesh) using a micropipette. The grid was allowed to dry under ambient conditions overnight in a dust-free environment to facilitate solvent evaporation. After drying, the grid was gently mounted onto the microscope stage for imaging. High-resolution TEM micrographs were captured to observe the size, shape, and dispersion of the nanoparticles. Additionally, selected area electron diffraction (SAED) patterns were acquired from individual regions of the grid to evaluate the crystalline structure and phase composition of the silver nanoparticles, confirming their polycrystalline nature.

2.5. Ellipsometry

The thickness of the plasma polymer films was determined using a Variable Angle Spectroscopic Ellipsometer (VASE; J.A. Woollam Co., Inc., Headquarters, Lincoln, NE, USA), equipped with an HS-190 high-speed monochromator and a VB-400 control module. All measurements were carried out at 5° intervals from 65° to 75°, with 10 nm increments, over a wavelength range of 250 to 1100 nm. WVASE32 software was used for data analysis. An inbuilt Cauchy algorithm was applied to fit the data.

2.6. Atomic Force Microscopy (AFM)

The topography of the POX, Ag-6h and Ag-24h surfaces was investigated by a Bruker Multimode 8-HR AFM in ScanAssist mode. A silicon nitride probe (SCANASYST-AIR, Bruker) with a force constant of 0.4 N m^{-1} and a 2–12 nm radius was used. The obtained images were analyzed using NanoScope Analysis 1.5 software.

2.7. Field Emission Scanning Electron Microscope (FESEM)

The surface morphology of POX, Ag-6h and Ag-24h surfaces was imaged using a Hitachi SU7000 ultra-high resolution FESEM (Hitachi, Tokyo, Japan). The imaging was conducted under an accelerating voltage of 2 kV to minimize sample charging and preserve surface integrity, while maintaining a working distance of 6 mm to optimize focus and depth of field.

2.8. UV-Visible Spectroscopy

The ultraviolet-visible (UV-Vis) absorption spectra of POX, Ag-6h and Ag-24h surfaces were recorded using a PerkinElmer Lambda 350 UV-Vis spectrophotometer (PerkinElmer, Hopkinton, MA, USA). Spectral acquisition was performed across a broad wavelength range of 200 to 900 nm, encompassing both the ultraviolet and visible regions, thereby capturing the key electronic transitions and surface plasmon resonance phenomena characteristic of these materials. This analysis aimed to evaluate changes in the optical properties due to silver incorporation and assess any time-dependent effects on the material's electronic structure, as indicated by potential shifts or changes in absorbance intensity at specific wavelengths.

2.9. Water Contact Angle

Static water contact angles of POX, Ag-6h, and Ag-24h surfaces were calculated using the sessile drop method, which involves depositing a 2 µL water droplet (Milli-Q) onto the sample surface with the RD-SDMO2 goniometer. The contact angles were calculated using the DropSnake plugin toolbar available in ImageJ software, version 1.54i (NIH, Bethesda, MD, USA).

2.10. Zeta Potential

The surface charge characteristics of POX, Ag-6h and Ag-24h surfaces were quantified by determining their zeta potential using the ZPA 2.0 instrument (DataPhysics Instruments GmbH, Filderstadt, Germany). This instrument uses the streaming potential method, specifically designed to analyze flat, planar substrates. Before measurement, all samples were thoroughly rinsed with Milli-Q water and dried under a nitrogen stream to remove residual ions or contaminants. Each sample was then mounted in the instrument's clamping cell, and an electrolyte solution (3 mM KCl) was flowed through a narrow slit formed by two parallel sample surfaces. The zeta potential (ζ) of the plasma-polymer-coated and AgNP-functionalized surfaces was determined by measuring the streaming potential generated between two parallel-mounted samples during electrolyte flow.

2.11. X-ray Photoelectron Spectroscopy (XPS)

The chemical compositions of POX, Ag-6h and Ag-24h surfaces were evaluated using a Kratos AXIS Ultra DLD spectrometer (Kratos Analytical, Manchester, UK). XPS spectra were obtained using a monochromatic Al Kα radiation source operated at 15 mA and 15 kV. The survey spectra were collected at a pass energy of 160 eV with a resolution of 0.5 eV, spanning the range of 0–1100 eV. High-resolution spectra were recorded with a pass energy of 20 eV. The data collected was analyzed using Casa XPS software (Version 2.3.25).

2.12. ICP-MS Analysis

The release of silver from POX, Ag-6h and Ag-24h well plates was quantified using an Agilent 8800 Triple Quad inductively coupled mass spectroscopy (ICP-MS, Agilent Technologies, Clara, CA, USA). Release studies were conducted in PBS at pH 7.4 and Milli-Q water in each well of treated 24-well plates. After 6, 24 and 168 h, the released silver in PBS and water was dissolved in dilute 2.8% HNO_3, and the silver concentration was evaluated using ICP-MS.

2.13. Assessment of Antibiofilm and Antimicrobial Efficacy

Four bacterial strains, *S. aureus* (ATCC 29213), *S. epidermidis* (ATCC 35984), *E. coli* (ATCC 25922), and *P. aeruginosa* (NCTC 6749), were selected for antibacterial testing due to their clinical relevance as common

causative agents of healthcare-associated infections [44–48]. The selected bacterial strains were plated on nutrient agar plates from frozen stocks maintained at −80 °C before each bacterial experiment. Fresh bacterial suspensions were prepared by growing isolated bacterial colonies at 37 °C in sterile TSB to mid-log phase (OD_{600nm} ~ 0.5), previously determined to correspond to approximately 5×10^7 CFU/mL. The bacterial suspension was then diluted to 1×10^6 CFU/mL using sterile TSB. Next, 400 µL of bacterial culture (1×10^6 CFU/mL) was added to each well of 24-well plates (treated and untreated) and incubated for 4 h. The next step was the addition of 400 µL of sterile TSB, which replaced the bacterial suspension in the wells. A second incubation was conducted for 24 h at 37 °C. After the second incubation, TSB from each well was collected and stored to determine the viable cell count. The wells were washed twice with 400 µL of sterile saline (0.9% sodium chloride) to ensure that only the attached biofilms remained. Ethanol-soaked swabs (70%) were used to clean the biofilm formed on the unexposed, untreated side of the samples. 400 µL of safranin (0.1%) was added to each well to stain the biofilms that adhered to the surface. After 15 min of incubation with the safranin, the wells were rinsed twice with 400 µL of sterile Milli-Q water to remove excess safranin and samples were allowed to dry at room temperature. Biofilms were imaged immediately after the Milli-Q water wash; the bacterial cells were then lysed with 400 µL of 33% acetic acid for 15 min to solubilize the adhered safranin. Finally, 100 µL of the content from each well was transferred into a 96-well plate, and the optical density (OD) was measured using a microplate reader (BioTek, Winooski, VT, USA) at 490 nm.

2.14. Zone of Inhibition

To measure the ZOI, 100 µL of each bacterial suspension (1×10^6 CFU/mL) prepared using sterile TSB was poured onto the surface of a separate nutrient agar plate and spread uniformly with a sterile spreader. The tests (Ag-6h and Ag-24h) and control samples were placed on Thermanox coverslips and incubated overnight at 37 °C. The ZOI was measured by subtracting the sample diameter from the total inhibition zone diameter.

2.15. Assessment of In Vitro Cytotoxicity

Cell viability on human foreskin fibroblasts (HFFF2, Catalog Number 86031405-1VL, Sigma-Aldrich (St. Louis, MO, USA) was evaluated by resazurin assay. HFFF2 cells were seeded onto each well of plasma-functionalized 24-well plates at a density of 1×10^5 cells in DMEM containing 5% fetal bovine serum (FBS) and 1% (*v*/*v*) penicillin/streptomycin. After 24 and 48 h of incubation at 37 °C, 5% CO_2 and 95% humidity, the media were removed, and 600 µL of the diluted (1:10) resazurin solution (stock concentration of 110 mg/mL) was added to each well. After 2 h incubation at 37 °C, the supernatant was transferred to a 96-well plate, and fluorescent intensity was recorded using a plate reader at an excitation wavelength of 544 nm and an emission wavelength of 590 nm. The percentage of cell viability was calculated using Equation (1).

$$\text{Viability (\%)} = 100 \times (F_t/F_c) \quad (1)$$

where F_t and F_c are the fluorescence intensities of the test and control samples, respectively.

For immunofluorescence staining, cells were first fixed using 4% paraformaldehyde in PBS for 15 min. They were then treated with 0.5% Triton X-100 (in PBS) for another 5 min. This was followed by three washes with PBS, followed by staining with 0.165 µM Alexa Fluor 488 phalloidin and 0.365 µM DAPI for 30 min in the dark. They were further washed in PBS and imaged using an Olympus IX83 Fluorescence Microscope (Olympus, Tokyo, Japan).

2.16. Inflammatory Response

The RAW 264.7 macrophage cell line (ATCC TIB-71, In Vitro Technologies, Noble Park, VIC, Australia) was used in this study and maintained according to the American Type Culture Collection (ATCC) protocol. RAW cells were maintained in DMEM supplemented with 5% heat-inactivated FBS and 1% (*v*/*v*) penicillin/streptomycin at 37 °C, 5% humidity and 5% CO_2. Cell passage was performed by detaching them from the flask using a scraper. The cells were expanded through two passages before being used in the subsequent experiments. Cells were seeded on all samples at a density of 1×10^5. Lipopolysaccharide (LPS) was added at a concentration of 1 µg/mL to stimulate the inflammatory response in macrophages for 2 h, a widely established protocol for inducing pro-inflammatory activation through Toll-like receptor 4 (TLR4) signaling pathway [49,50]. After 6 h of culturing on different surfaces, TRIzol reagent was used to extract the total RNA from the treated RAW cells. Gene expression of inflammatory cytokines (IL-1β and IL-6), macrophage phenotype markers (CCR7, iNOS and CD86), osteogenesis-related cell signaling pathways (Smad1, Smad5, and BMPR1a), and osteoclastogenesis-related markers (TRAP, CTSK, CSF1, and CAR2) was assessed by RT-qPCR. Complementary DNA was synthesized

from 500 ng of total RNA using a SensiFAST™ cDNA Synthesis Kit, after following the manufacturer's instructions. The information about the used RT-qPCR primers is provided in the supporting information (Table S1). The relative expression levels were determined by normalizing the cycle threshold (Ct) value of each target gene against the Ct value of a housekeeping gene (18S). The ΔΔCt method was used to calculate the fold change and compare the mRNA expression levels of the treatment groups (POX, Ag-6h, Ag-24h) with those of the negative control group. The samples were sputter-coated with platinum-palladium (5nm) and the macrophage morphology on different surfaces was examined using a Zeiss SEM (FEI, USA). An ELISA was used to measure the secretion of IL-6 and TNF-α in the supernatants, according to the manufacturer's instructions. The absorbance at 450 nm was measured using a Bio-Rad microplate absorbance spectrophotometer with a reference absorbance at 570 nm. The concentrations of cytokines were quantified from the standard curve.

2.17. Osteogenic Studies

This study used the macrophage cell line RAW 264.7 and human bone marrow mesenchymal stromal cells (hBMSCs) isolated in our laboratory [51,52]. The Human Ethics Committee at Queensland University of Technology approved handling human subject samples (QUT 1600000183 and TPCH EC2310). The indirect co-culture of hBMSCs and macrophages was performed using 6-well transwell inserts with 0.4 μm pores, following the guidelines proposed by Chen et al. [53]. Macrophages were seeded at 1×10^5 cells/well onto POX, Ag-6h, Ag-24h, and control surfaces in the upper chamber, while hBMSCs were seeded at 1×10^5 cells/well in the lower chamber. The co-culture was incubated for 3 days at 37 °C, 5% CO_2 and 95% humidity. Subsequently, the expression of osteogenic-related genes (OCN, OPN, COL1, E11, BSP), SMAD signaling pathway-related genes (BMPR1A, BMPR1B, Smad1, Smad4, Smad5, Smad8), angiogenesis-related gene (VEGF), and WNT signaling pathway-related genes (WNT5a, WNT5b, WNT10b) was determined using RT-qPCR.

2.18. Immunofluorescence Staining for Detection of Osteogenesis-Related Protein (OPN)

Immunofluorescence staining was performed to detect the protein expression of OPN. Cells were fixed, permeabilized, and blocked with 2% BSA for 1 h at room temperature before incubation with the primary antibody overnight at 4 °C. Alexa Fluor® 488 anti-rabbit IgG secondary antibody (1:1000) was used as the secondary antibody. Images were captured using a confocal laser scanning microscope (Nikon A1R Confocal, Nikon, Tokyo, Japan).

2.19. Statistical analysis

GraphPad Prism 6.07 (GraphPad Software, CA, USA; www.graphpad.com) was used for statistical analysis, and data were reported as mean ± standard deviation (SD). A one-way ANOVA test was performed to determine statistical significance, followed by Tukey's post hoc test for multiple comparisons. All experiments were performed in triplicate, and a *p*-value of less than 0.05 was deemed statistically significant.

3. Results

3.1. Coatings Preparation and Characterization

A schematic depicting the fabrication of generating substrate-independent antibacterial coatings is shown in Figure 1a,b. First, a thin plasma polymer coating from the vapor of 2-methyl 2-oxazoline was deposited. The coatings had a thickness of 25.0 ± 0.3 nm as determined by spectroscopic ellipsometry. An AFM image of the surface of the plasma polymer coating of the supplementary material is shown in Figure S1. The coatings are very smooth, uniform and pinhole-free. The coated samples were then immersed in a solution of AgNPs@MSA for 6 and 24 h. This time-dependent experiment aimed to produce substrates with two different surface concentrations of immobilized silver nanoparticles (Ag-6h and Ag-24h). The immersion of a POX-coated substrate in a solution of AgNPs@MSA results in covalent binding of the nanoparticles to the surface. The AgNPs@MSA particles possess carboxyl acid functional groups on their outer surface, which spontaneously react with the population of oxazoline rings on the surface of the plasma polymer coatings to form a covalent bond [31,32,37]. After nanoparticle deposition, the surface acquires the typical yellow-brownish color caused by the plasmon resonance adsorption of the AgNPs@MSA (Figure 1b). This was supported by a characteristic surface plasmon resonance peak of AgNPs@MSA at around 435 nm in the case of Ag-6h and Ag-24h, which was absent in the POX coating and on the bare substrate (Figure 1i). The intensity of the absorption peak was higher for Ag-24h than for Ag-6h, which can be attributed to the greater number of AgNPs after 24h of immobilization. The surface charge also decreased after the immobilization of AgNPs due to the dissociation of the carboxylic acid group of MSA on the AgNPs surface. As

expected, the zeta potential was a greater negative value for Ag-24h than for Ag-6h, at −73 ± 3 mV and −64 ± 2mV, respectively (Figure 1j).

SEM and AFM inspections of the surfaces demonstrated uniform nanoparticle coverage and absence of aggregations (Figures 1f–h and S1). The TEM images of AgNPs@MSA showed that the size of the nanoparticles is 12.0 ± 1.3 nm (Figure 1c,e), consistent with our previous studies where we reported the synthesis of this particular type of nanoparticles [26,54]. The SAED pattern confirmed that particles are polycrystalline with concentric diffraction rings around (111), (200), and (220) planes of the face-centred cubic crystalline lattice of silver (Figure 1d). The wettability of the surfaces was evaluated from static water contact angles (WCA). After surface immobilization, the hydrophilicity of the surfaces increased, leading to a reduction of WCA after AgNPs@MSA immobilization (Figure 1k).

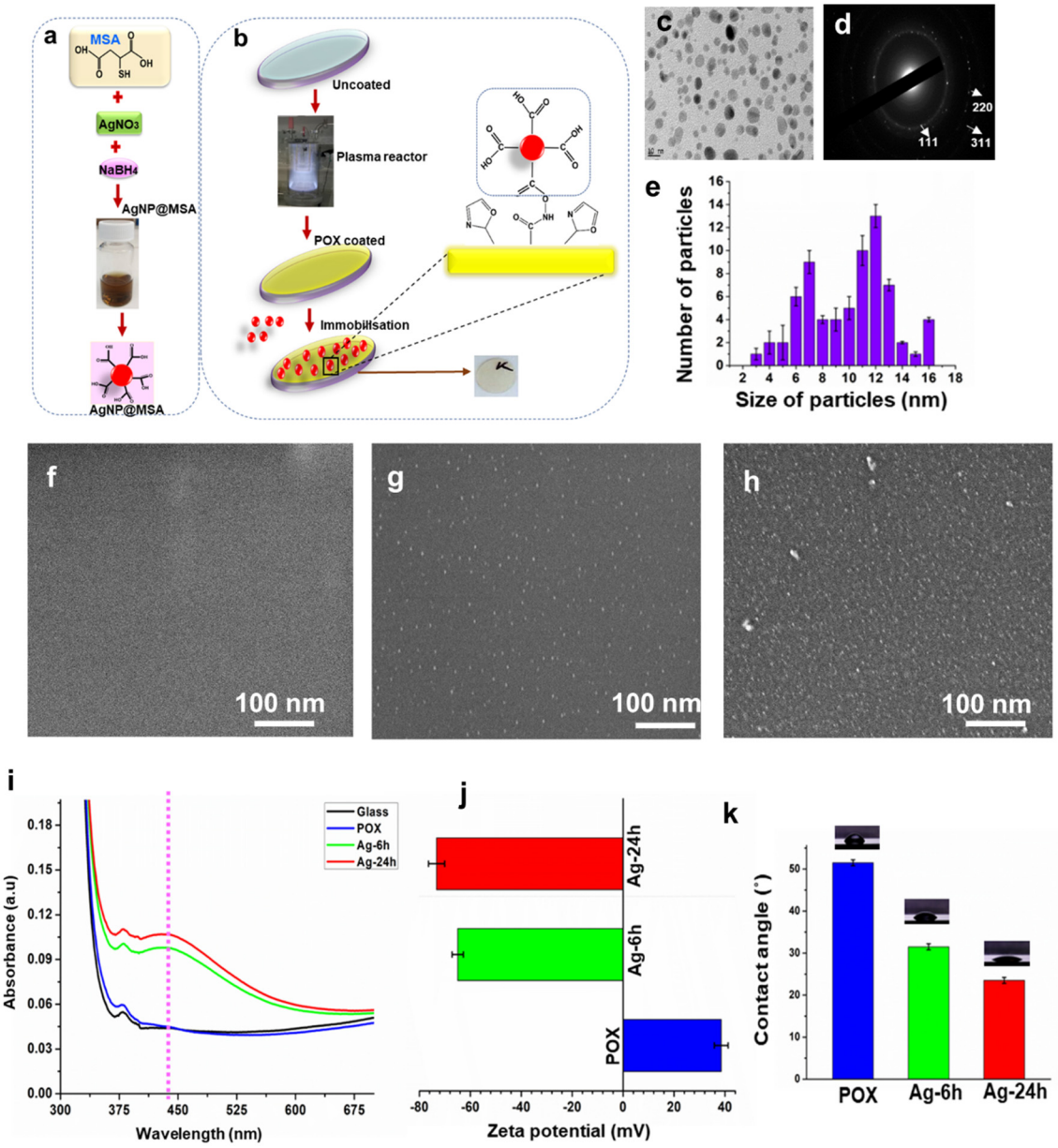

Figure 1. (**a**) Schematic representation illustrating the synthesis of AgNPs@MSA and (**b**) fabrication of plasma coated substrate immobilized with AgNPs@MSA; (**c**) TEM, (**d**) SAED and (**e**) particle size distribution of AgNPs@MSA; SEM images of (**f**) POX, (**g**) Ag-6h and (**h**) Ag-24h; (**i**) UV visible spectra of glass, POX, Ag-6h and Ag-24h; (**j**) Zeta potential analysis of POX, Ag-6h and Ag-24h (**k**) Water contact angle of POX, Ag-6h and Ag-24h. Data plotted as mean ± SD and $n = 3$.

The chemical composition of the AgNPs@MSA-coated samples and POX was characterized by XPS, as shown in Figure 2. On POX-coated samples, a distinct nitrogen (N1s) peak, along with oxygen and hydrogen, appears in the survey spectrum, consistent with the precursor's chemical composition (Figure 2a). Immobilization

of AgNPs@MSA results in a strong signal corresponding to electrons ejected from the 3d orbital of silver. Figure 2b shows that the atomic percentage of silver increased from 9 ± 0.5% for Ag-6h to 14 ± 1% for Ag-24h, confirming greater AgNPs concentration after 24 h of immobilization.

The high-resolution C1s spectra of POX, Ag-6h and Ag-24h reveal characteristic peaks representing various carbon environments. The deconvoluted spectra display peaks at C-C/C-H (at 285 eV), C-N/C-O (at 286–286.5eV), N-C=O (at 288.2 eV), O-C=O bonds (at 289 eV) and beta shift component, O-C=Ob (at 285.5 eV), which can be attributed to the various chemical functionalities in the POX coating and the immobilized silver nanoparticles. The increased At percentage of O-C=O bonds Ag-6h and Ag-24h compared to POX is due to the immobilization of AgNPs@MSA onto POX (Figure 2c–e). As expected, the At% of O-C=O bonds is greater in Ag-24h compared to Ag-6h due to greater AgNPs@MSA on the surface.

Silver oxidizes in the presence of moisture and oxygen, releasing silver ions into aqueous environments that can kill bacteria [55]. This dissolution process would eventually result in the loss of silver from the surface. To examine the rate at which silver is lost from the coating developed in this work, the samples were immersed in aqueous media (water and PBS) for 168 h (Figure 2f,g). The release of silver was higher in PBS than in water, probably due to complexation of phosphate and chloride ions in PBS, increasing the dissolution of silver ions [56]. As expected, a greater concentration of silver ions was released from Ag-24h compared to Ag-6h. The stronger covalent bond between the nanoparticles and the plasma polymer film appears beneficial for retaining silver on the coatings' surface for a longer time, allowing a slow and concentration-dependent release of silver ions.

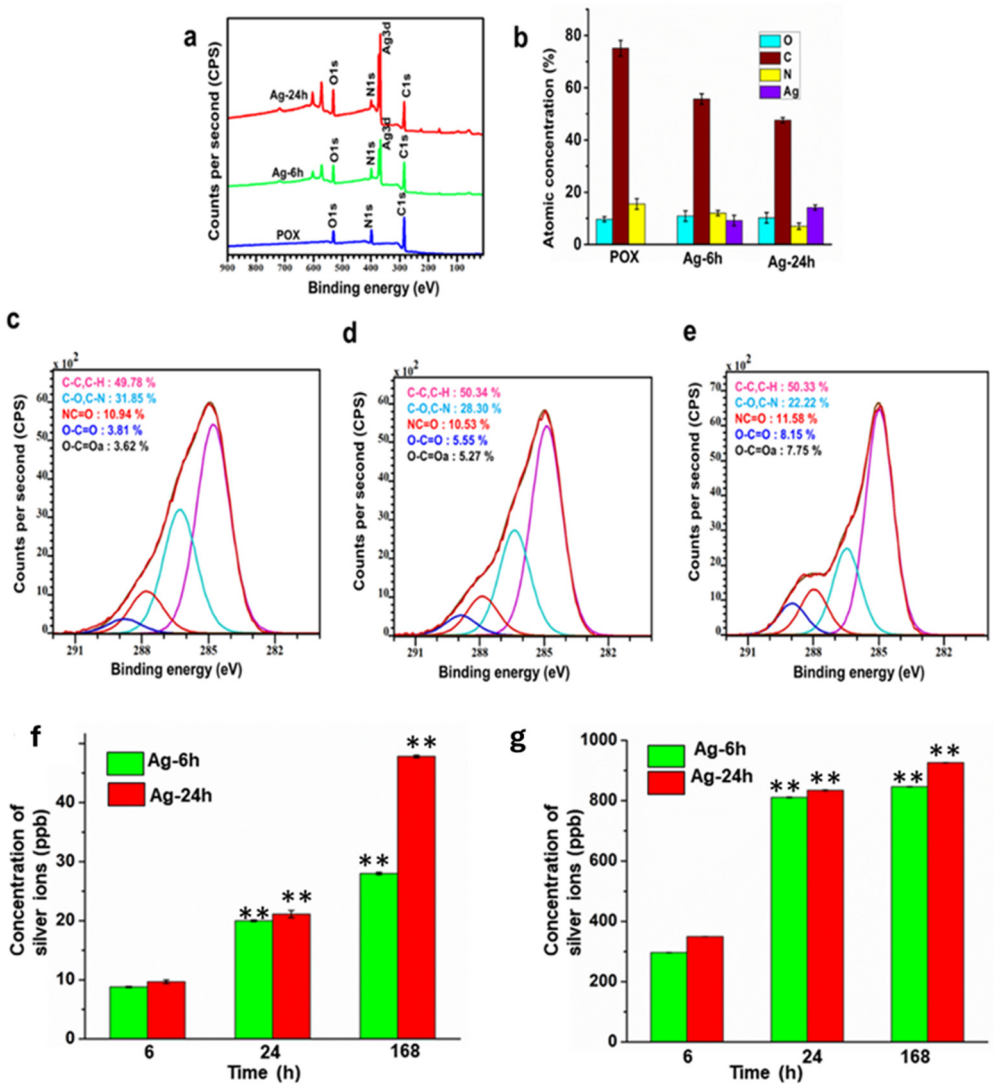

Figure 2. (**a**) X-ray photoelectron spectroscopy survey spectra, and (**b**) Atomic percentage of elements of POX, Ag-6h and Ag-24h, data plotted as mean ± SD and $n = 3$; high-resolution C1s spectra of (**c**) POX, (**d**) Ag-6h and (**e**) Ag-24h. Silver release from Ag-6h and Ag-24h was quantified by ICP-MS after 6, 24, and 128 h in (**f**) Milli Q water and (**g**) PBS. Data plotted as mean ± SD, $n = 3$ and ** $p < 0.01$.

3.2. Antibacterial Efficacy

The antibacterial capacity of the coatings was tested in the culture of pathogens often associated with medical device-related infections. We used *S. aureus* and *S. epidermidis* as Gram-positive organisms, while *E. coli* and *P. aeruginosa* were selected as Gram-negative organisms. It is important to note that the bacterial concentration used for incubation was 10^6 CFU/mL, substantially higher than typical contamination levels found on medical device surfaces in hospital settings [57,58].

3.3. Quantification of Bacterial Biofilm

Biofilm formation was quantified by culturing the bacteria for 24 h on the POX coating, AgNPs@MSA-modified surfaces and controls, followed by staining with safranin-O. Two surface concentrations of surface-bound AgNPs@MSA were selected for these studies, denoted as Ag-6h and Ag-24h, corresponding to 9 ± 0.5% and 14 ± 1%, respectively, At% of silver as measured by XPS. SEM images of the morphology of these samples are presented in (Figure 1f–h), showing the greater concentration of AgNPs@MSA after 24h of immobilization and consistent with the silver atomic concentration determined by XPS. Quantification of the intensity of safranin staining (for biofilm) relative to the control (uncoated cell culture well) and the corresponding images of the wells after staining are presented in Figure 3a–d. The plasma polymer coating (POX) demonstrated notable antibacterial activity, reducing biofilm formation. This finding is consistent with our early work on this type of coating, where we reported that bacteria could not form biofilms [33], The mechanistic picture of why bacteria cannot form biofilms on plasma-polymerized oxazoline-based films is yet to be fully understood; however, the coating appears to be very useful for coating medical device surfaces. Adding AgNPs@MSA further reduced bacterial surface attachment, as shown in Figure 3a. A simple visual inspection of the surfaces where AgNPs@MSA were immobilized showed a nearly complete absence of the red color, indicating the elimination of biofilm development (Figure 3a). This demonstrates the added benefit of a high surface concentration of silver ions, delivered via covalently attached AgNPs@MSA, in enhancing the antibacterial efficacy of the plasma polymer coating, depicted in Figure 3e.

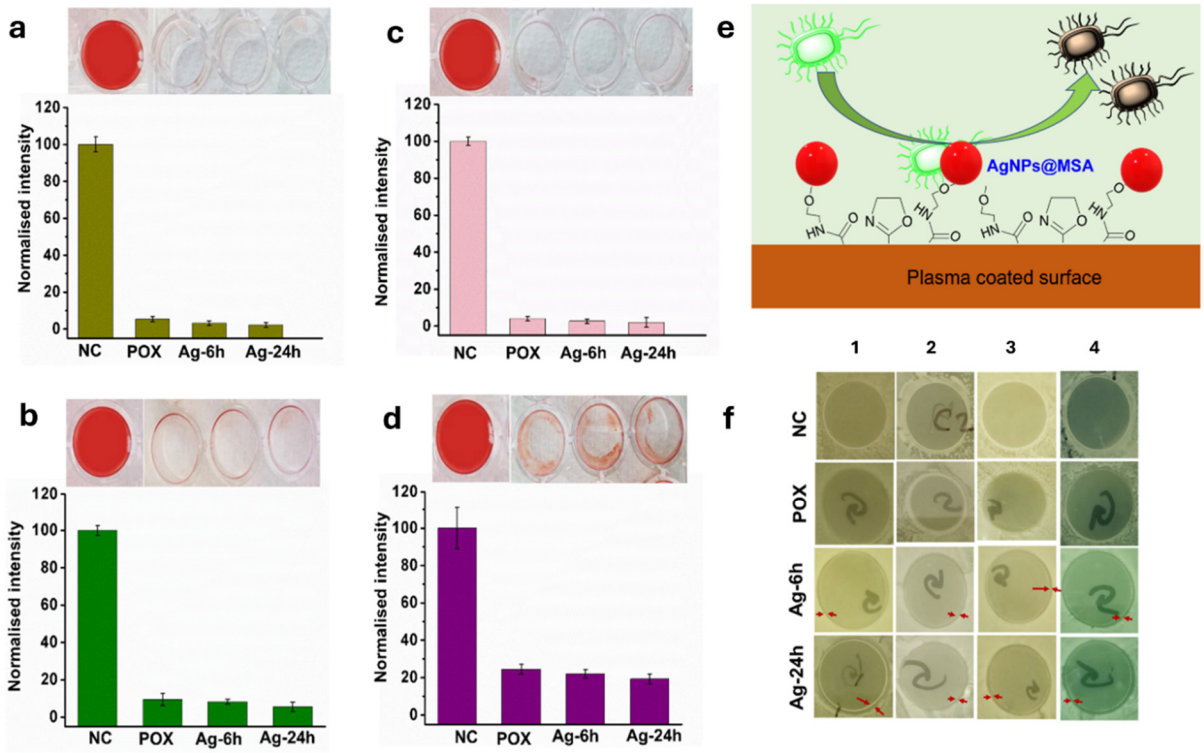

Figure 3. Antibacterial tests: Intensity of safranin-O staining for biofilm after 24 h incubation in a culture of (**a**) *E. coli*, (**b**) *P. aeruginosa*, (**c**) *S. epidermidis*, (**d**) *S. aureus*, and corresponding images of the cell culture wells of uncoated (control), POX, Ag-6h and Ag-24h. Data plotted as mean ± SD and $n = 3$ (**e**) Schematic illustration of antibacterial effect of POX-coated surfaces immobilized with AgNPs@MSA (**f**) Zone of inhibition assay of uncoated coverslips POX, Ag-6h and Ag-24h against bacterial strains, including (**1**) *E. coli*, (**2**) *S. epidermidis*, (**3**) *P. aeruginosa*, (**4**) *S. aureus.*

3.4. Zone of Inhibition Assay

The purpose of adding AgNPs@MSA to the oxazoline-derived plasma polymer coatings was to achieve antibacterial capacity on both the coated surface and in its vicinity. We conducted a disc diffusion assay with *S. epidermidis*, *P. aeruginosa*, *S. aureus*, and *E. coli* to test the hypothesis that silver ions released from the nanoparticles will accomplish this goal. Thermanox coverslips were coated with POX and AgNPs@MSA (Ag-6h and Ag-24h) for this experiment. Results are shown in Figure 3c. Samples with immobilized AgNPs@MSA exhibited a clear inhibition zone with an annular radius ranging from 1.4 to 3.3 mm against the four bacterial strains (Table S2), demonstrating the silver ion release capacity to eliminate bacteria near the substrate (Figure S2). The control coverslip and those coated with POX (without AgNPs@MSA) did not produce any inhibition zone (Figure 3f). This discrepancy reflects different mechanisms: POX prevents bacterial adhesion and biofilm formation through antifouling surface properties, but does not release antibacterial agents, hence no inhibition zone is observed [59]. This assay confirms that the antibacterial efficacy of the plasma polymer coating is further improved after the covalent immobilization of AgNPs@MSA.

3.5. Cytotoxicity

It is vital to ensure that medical device coatings are not only antibacterial but also nontoxic to human cells and tissue [60–63]. The cytotoxicity of the coatings was evaluated in a culture of primary human foreskin fibroblasts (HFFF2). HFFF2 plays a role in wound healing and tissue repair and is often used as a model to assess biocompatibility [64,65]. POX, Ag-6h and Ag-24h were tested against the uncoated well plate. The viability of the cells was evaluated via the resazurin assay, in which live cells convert resazurin to resorufin. No significant reduction in cell viability was noted in any of the tested samples after 24 h and 48 h. Fluorescence imaging was performed following cell fixation and staining with phalloidin for actin filaments and DAPI for nuclei. The cells had an elongated shape typical of fibroblasts, with no abnormalities noted (Figure 4a). These results showed that, despite being highly toxic to bacteria, the coatings containing AgNPs@MSA exhibited no significant cytotoxicity to HFFF2, indicating their suitability for biomedical applications (Figure 4b). Together, these findings support the dual functionality of the coatings, which combine strong antibacterial efficacy with excellent cytocompatibility, which are key attributes for the safe and effective use of medical devices.

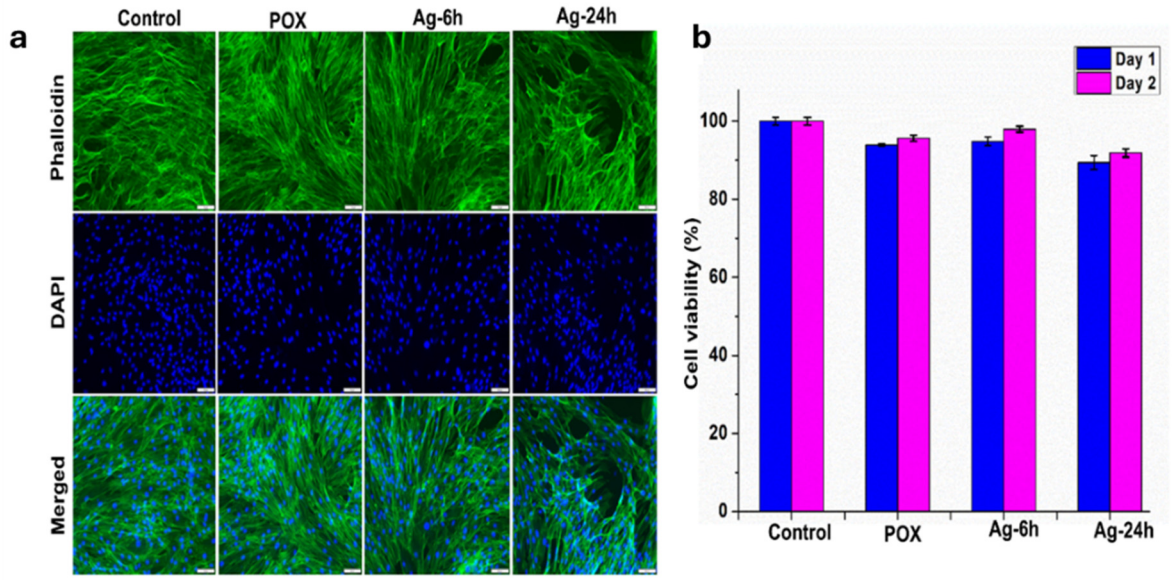

Figure 4. (**a**) Fluorescent microscopy images of untreated HFFF2 cells (control) and cells treated with POX, Ag-6h and Ag-24h and their (**b**) viability analysis after 24 and 48 h. Data plotted as mean ± SD and n =3.

3.6. Immunomodulatory Responses

We then focused on understanding the physiological processes associated with using the coatings developed in this work on medical devices. The inflammatory response to any foreign material is a critical factor. To understand the possible innate immune response to the coatings developed in this work, we conducted studies involving macrophages and measured the expression levels of inflammatory genes (Figure 5a,b). Cells cultured

on control surfaces after LPS stimulation showed flattened morphology. The elongation of macrophages on Ag-24h was more pronounced than that of cells cultured on the Ag-6h and POX surfaces. ELISA further evaluated the release of inflammatory cytokines (IL-6 and TNF-α). As shown in Figure 5c, the production of inflammatory cytokines was significantly reduced following treatment with Ag-6h and Ag-24h ($p < 0.05$). The expression of inflammatory cytokines (IL-1β and IL-6), macrophage phenotype markers (CCR7, iNOS and CD86), osteogenesis-related cell signaling pathways (Smad1, Smad5, and BMPR1a), and osteoclastogenesis-related markers (TRAP, CTSK, CSF1, and CAR2) was assessed by RT-qPCR (Figure 5d). The gene expression of inflammatory cytokines (IL-1β and IL-6), macrophage phenotype markers (CCR7, iNOS and CD86), and osteoclastogenesis-related markers (TRAP, CTSK, CSF1, and CAR2) was significantly lower when macrophages were cultured on AgNPs@MSA immobilized surface ($p < 0.05$). These results suggest that AgNPs@MSA functionalized surfaces not only mitigate pro-inflammatory signaling but also promote a more regulated immune environment, thereby creating favorable conditions for downstream tissue healing and osteointegration in medical device applications.

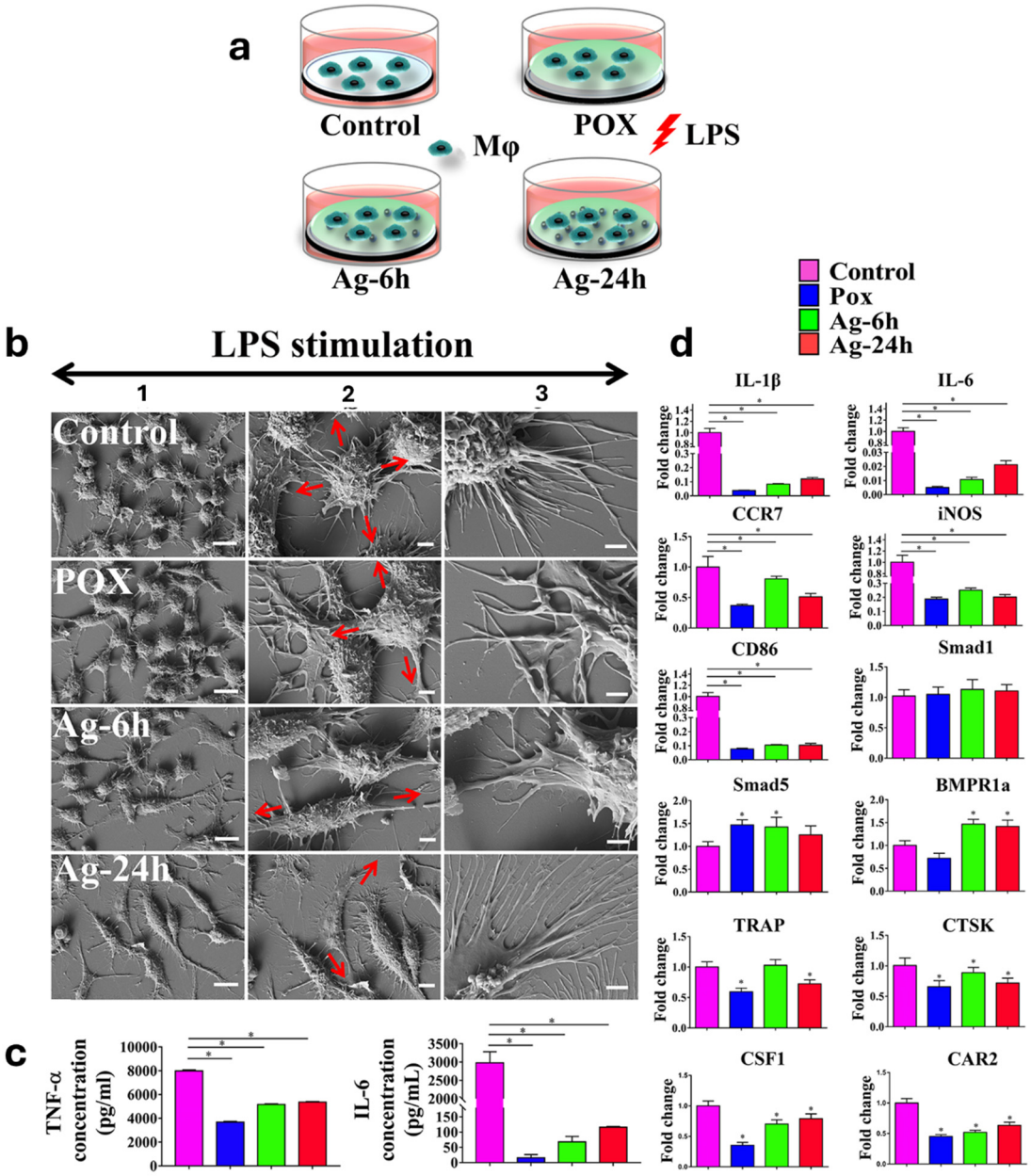

Figure 5. Inflammatory responses of macrophages stimulated by surface chemistry and silver nanotopographies. (**a**) Experimental protocol of the macrophage inflammatory response study. 1 μg/mL lipopolysaccharide (LPS) created an inflammatory environment. (**b**) Representative SEM images of RAW 264.7 cells cultured on control, POX, Ag-6h, and Ag-24h surfaces under an inflammatory environment. All scale bars: 10 μm (**1**), 2 μm (**2**), and 1 μm (**3**). (**c**) Expression profiles of IL-6 and TNF-α produced in RAW 264.7 cells cultured on control, POX, Ag-6h, and Ag-24h

surfaces. The levels of IL-6 and TNF-α were measured using cytokine-specific ELISA. All data are expressed as mean ± SD. (**d**) Gene expression of pro-inflammatory genes (IL-1β, IL-6, CCR7, iNOS, and CD86), SMAD signalling pathway (SMAD1, SMAD5, and BMPR1A), and osteoclastogenesis-related genes (TRAP, CTSK, CSF1, and CAR2) detected by qRT-PCR. The expression of inflammatory-related genes in AgNPs@MSA immobilized surfaces was significantly decreased. Data plotted as mean ± SD, $n = 3$ and * $p < 0.05$. Statistical analysis was performed across all groups (Control, POX, Ag-6h, Ag-24h); for clarity, only the most relevant comparisons are annotated in the figure, while all pairwise comparisons were assessed.

3.7. AgNPs@MSA Coating Enhanced the In Vitro Osteogenesis via Modulating the Macrophage Immune Response

Since many implantable devices, such as dental, hip and knee implants, require osteointegration, we examine how the antibacterial surfaces generated in this work affect osteogenesis. Figure 6a illustrates the experimental procedure used to assess the effects of different surface coatings on cell behavior in a co-culture model. There was no significant morphological difference between hBMSCs. However, cells presented more intense OPN staining in the Ag-6h group compared to the control (Figure 6b). mRNA expression of osteogenic-related genes (OCN, OPN, COLI, E11 and BSP), Smad pathway-related genes (BMPR1A, BMPR1B, Smad1, Smad4, Smad5 and Smad8), and Wnt signaling pathway-related genes (Wnt5a, Wnt5b and Wnt10b) were further determined by RT-qPCR (Figure 6c). The results showed that hBMSCs co-cultured with macrophages on Ag-6h and Ag-24h surfaces exhibited upregulation of osteogenic genes and activation of the Smad and Wnt/β-catenin signalling pathways. Although the increase with Ag-24h did not reach statistical significance, the effect was more pronounced with Ag-6h, indicating that shorter silver exposure more effectively promotes a pro-osteogenic environment through macrophage-mediated signalling ($p < 0.05$).

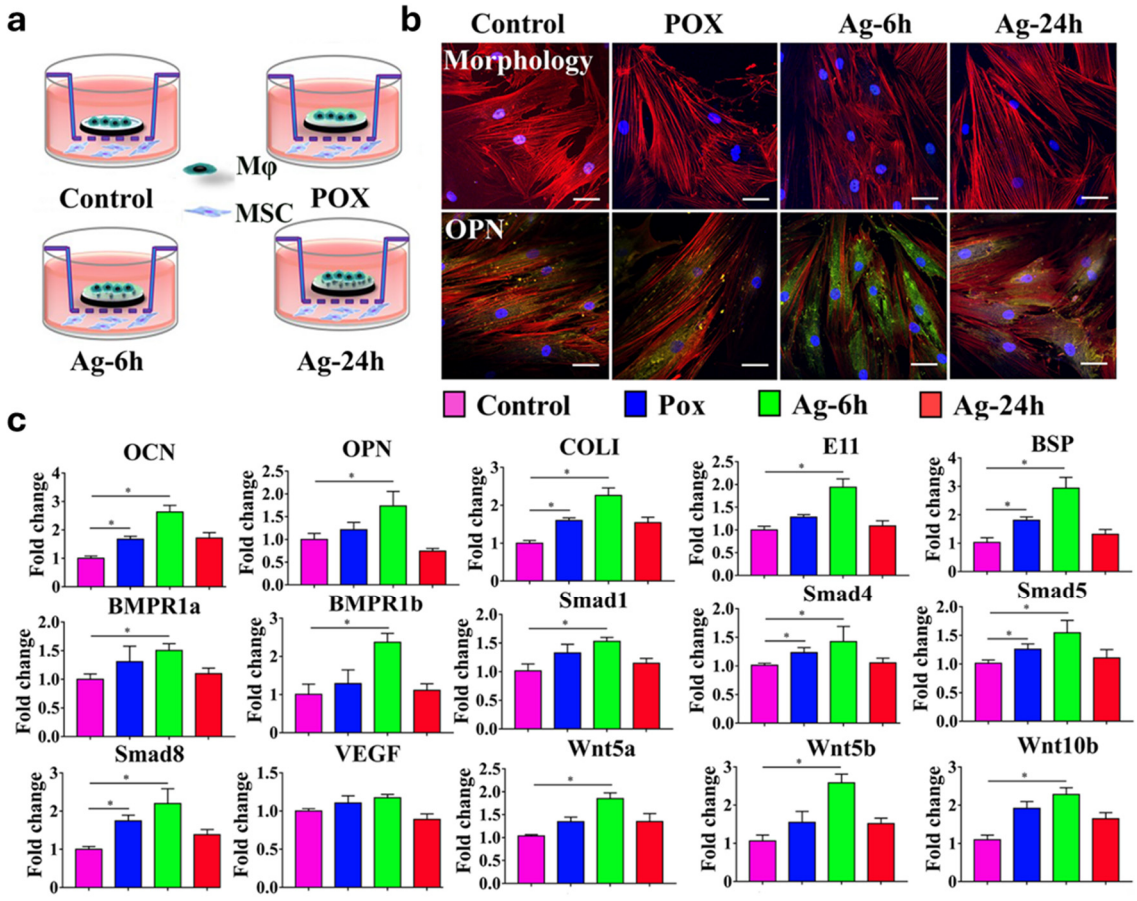

Figure 6. AgNPs@MSA enhanced in vitro osteogenesis by modulating the macrophages' immune response. (**a**) Experimental protocol of the indirect co-culture study. RAW264.7 cells seeded on control, POX, Ag-6h, and Ag-24h surfaces were placed on a 0.4 μm hanging cell insert, while hBMSCs were cultured in the lower chamber. (**b**) Representative confocal microscopy images of hBMSCs morphology (**a**) and OPN expression. All scale bars: 50 μm. (**c**) mRNA expression of osteogenic-related genes (OCN, OPN, COLI, E11, and BSP), Smad pathway-related genes (BMPR1A, BMPR1B, Smad1, Smad4, Smad5, and Smad8), and Wnt signalling pathway-related genes (Wnt5a,

Wnt5b and Wnt10b). Data plotted as mean ± SD, $n = 3$ and * $p < 0.05$. Statistical analysis was performed across all groups (Control, POX, Ag-6h, Ag-24h); for clarity, only the most relevant comparisons are annotated in the figure, while all pairwise comparisons were assessed.

The AgNP-coated substrates demonstrated potent antibacterial and antibiofilm activity against Gram-negative and Gram-positive pathogens, effectively preventing bacterial adhesion and suppressing biofilm development. This broad-spectrum efficacy highlights their potential for reducing microbial colonization and infection on biomaterial surfaces.

Interestingly, AgNPs@MSA surfaces significantly reduced macrophage activation compared to the control group. This was evident from the cell morphology, lower TNF-α and IL-6 secretion, and downregulation of pro-inflammatory genes (IL-1β, iNOS, CD86). Concurrently, upregulation of Smad1, Smad5, and BMPR1a suggests a shift toward an anti-inflammatory or reparative phenotype. These results suggest silver treatments can mitigate inflammatory responses and potentially promote tissue regeneration [66–68].

Among the tested conditions, the Ag-6h treatment most effectively promoted the osteogenic differentiation of MSCs. This group exhibited the highest expression levels of key osteogenic markers, including OCN, COL1, E11, and BSP, indicating enhanced maturation toward the osteoblastic lineage. Ag-6h also showed stronger activation of the BMP signalling pathway, with elevated expression of BMPR1a, BMPR1b, Smad1, Smad4, and Smad5, as well as increased expression of Wnt5a and Wnt5b, suggesting synergistic activation of osteogenic pathways. Immunostaining further supported these findings, with more intense OPN expression in the Ag-6h group. Collectively, these results highlight Ag-6h as the most effective treatment for promoting a pro-osteogenic environment. Our results are consistent with earlier studies, which also confirmed that low-dose AgNPs enhanced the gene expression of osteogenesis genes by our team and others [39–41,69].

Collectively, the superior performance of Ag-6h likely arises from an optimal silver ion release profile that strikes a balance by providing potent elimination of pathogens yet restrained enough to avoid interfering with immune regulation and bone regenerative processes.

4. Discussion

In this work, we developed a multifunctional plasma-coated surface with outstanding potential. Its substrate-independent nature allows it to be applied across various biomaterial substrates without compromising functionality. This adaptability is helpful in biomedical industry applications, where biomaterials often differ in composition. The ICP-MS data confirm controlled release of silver ions, while the covalent immobilization strategy makes detachment of intact AgNPs unlikely; nevertheless, future nanoparticle-specific analyses will be necessary to validate coating stability fully. These surfaces exhibited significant antibacterial potential to eradicate biofilm formation. They also differentiated osteocytes, which is ideal for bone tissue engineering. Particularly, the Ag-6h coating reached a balance between cytocompatibility and antibacterial potency, outpacing numerous earlier described coatings.

Our findings suggest that the coatings modulate macrophage responses by suppressing pro-inflammatory cytokines (IL-1β, IL-6, TNF-α) while promoting a reparative phenotype. Although direct pathway analysis was not performed, we hypothesize that inhibiting NF-κB and MAPK signaling may mediate these effects, which are key drivers of macrophage pro-inflammatory activation [70,71]. Concurrently, the observed upregulation of Smad 1, Smad 5, BMPR1a and Wnt/β-catenin pathway genes indicates a shift toward pro-osteogenic signaling, consistent with prior studies on immune–bone crosstalk [72,73]. In addition, controlled silver ion release and altered protein adsorption at the biointerface may further influence macrophage polarization, creating a local microenvironment favorable for osteogenesis [74].

Compared to other reported literature on chitosan/silver coating, hydroxyapatite coatings doped with silver and bioglass/ZnO composites, Ag-6h coatings exhibited superior antibacterial and osteogenic properties, stressing their use for clinical applications [75–77]. While the in vitro results are encouraging, future studies will focus on validating the coating in a rat femoral implant infection model, elucidating the immune-mediated mechanisms driving osteogenesis, fine-tuning silver release kinetics, long-term safety evaluations and adapting the platform to diverse clinically relevant implant surfaces to support its translation into practical therapeutic applications.

5. Conclusions

In summary, we have generated substrate-independent antibacterial coatings consisting of an intrinsically low-bacteria-fouling plasma polymer film and covalently attached silver nanoparticles functionalized with 2-mercaptosuccinic acid (AgNPs@MSA). The covalent immobilization was enabled by oxazoline functionalities

retained on the plasma polymer surface and carboxyl acid groups on the AgNPs@MSA, yielding a stable and durable surface modification. This design effectively inhibited biofilm formation and demonstrated strong antibacterial activity against medically relevant pathogens, including *S aureus*, *S. epidermidis*, *E. coli*, and *P. aeruginosa*. The zone of inhibition assay confirmed the release of bactericidal silver ions into the surrounding environment. Beyond antimicrobial properties, the coatings effectively modulated immune responses, attenuating pro-inflammatory cytokine expression in macrophages while promoting pro-osteogenic signalling in co-cultured bone marrow stromal cells. Among the tested conditions, Ag-6h (9 At% of Ag as measured by XPS) provided the optimal balance, as it maximized antibacterial activity and immunomodulatory effects while most effectively enhancing osteogenic gene expression and matrix protein deposition. These findings suggest that AgNPs@MSA-immobilized plasma polymer coatings hold considerable translational promise for orthopedic and dental implants, where infection control and bone integration are critical.

Supplementary Materials

The additional data and information can be downloaded at: https://media.sciltp.com/articles/others/25 09100854069887/RMD-2508000274-supplementary-FC.pdf.

Author Contributions

Conception and design—K.V. Development of methodology—N.N., R.B., F.W., K.V. and Y.Z. Acquisition of data—N.N., R.B., F.W. and D.P. Analysis and interpretation of data—N.N., R.B., F.W., P.Z., Y.X., Y.Z. and K.V. Writing, review, and/or revision of the manuscript—N.N., R.B., F.W., Y.X., P.Z. and K.V. Administrative, technical, or material support—Y.X., P.Z. and K.V. Study supervision—Y.X., R.B. and K.V. All authors have read and agreed to the published version of the manuscript.

Funding

This work was supported by the Australian Government Research Training Program Scholarship from the Australian Federal Government. Krasimir Vasilev thanks NHMRC for GNT1194466.

Institutional Review Board Statement

Not applicable.

Informed Consent Statement

Not applicable.

Data Availability Statement

The data is available upon reasonable request from the corresponding authors.

Conflicts of Interest

The authors declare no conflict of interest.

References

1. Darouiche, R.O. Treatment of infections associated with surgical implants. *N. Engl. J. Med.* **2004**, *350*, 1422–1429.
2. Rosenthal, V.D.; Al-Abdely, H.M.; El-Kholy, A.A.; et al. International Nosocomial Infection Control Consortium report, data summary of 50 countries for 2010-2015: Device-associated module. *Am. J. Infect. Control* **2016**, *44*, 1495–1504.
3. Vasilev, K.; Poulter, N.; Martinek, P.; et al. Controlled Release of Levofloxacin Sandwiched between Two Plasma Polymerized Layers on a Solid Carrier. *ACS Appl. Mater. Interfaces* **2011**, *3*, 4831–4836.
4. Dudeck, M.A.; Edwards, J.R.; Allen-Bridson, K.; et al. National Healthcare Safety Network report, data summary for 2013, Device-associated Module. *Am. J. Infect. Control* **2015**, *43*, 206–221.
5. Li, B.; Thebault, P.; Labat, B.; et al. Implants coating strategies for antibacterial treatment in fracture and defect models: A systematic review of animal studies. *J. Orthop. Transl.* **2024**, *45*, 24–35.
6. Zimlichman, E.; Henderson, D.; Tamir, O.; et al. Health Care–Associated Infections: A Meta-analysis of Costs and Financial Impact on the US Health Care System. *JAMA Intern. Med.* **2013**, *173*, 2039–2046.
7. Bleyer, A.J. Use of antimicrobial catheter lock solutions to prevent catheter-related bacteremia. *Clin. J. Am. Soc. Nephrol. CJASN* **2007**, *2*, 1073–1078.

8. Allegranzi, B.; Bagheri Nejad, S.; Combescure, C.; et al. Burden of endemic health-care-associated infection in developing countries: Systematic review and meta-analysis. *Lancet* **2011**, *377*, 228–241.
9. Deen, J.; von Seidlein, L.; Andersen, F.; et al. Community-acquired bacterial bloodstream infections in developing countries in south and southeast Asia: A systematic review. *Lancet. Infect. Dis.* **2012**, *12*, 480–487.
10. Bagheri Nejad, S.; Allegranzi, B.; Syed, S.B.; et al. Health-care-associated infection in Africa: A systematic review. *Bull. World Health Organ.* **2011**, *89*, 757–765.
11. Grayson, M.L. *Kucers' the Use of Antibiotics: A Clinical Review of Antibacterial, Antifungal, Antiparasitic and Antiviral Drugs*; CRC Press: Boca Raton, FL, USA, 2017.
12. Diab-El Schahawi, M.; Presterl, E.; Reilly, J.S. *Basic Microbiology and Infection Control for Midwives*, 1st ed.; Springer International Publishing: Cham, Switzerland, 2019.
13. Bright, R.; Hayles, A.; Wood, J.; et al. Surfaces Containing Sharp Nanostructures Enhance Antibiotic Efficacy. *Nano Lett.* **2022**, *22*, 6724–6731.
14. Shree, P.; Singh, C.K.; Sodhi, K.K.; et al. Biofilms: Understanding the structure and contribution towards bacterial resistance in antibiotics. *Med. Microecol.* **2023**, *16*, 100084.
15. Lim, L.M.; Ly, N.; Anderson, D.; et al. Resurgence of colistin: A review of resistance, toxicity, pharmacodynamics, and dosing. *Pharmacotherapy* **2010**, *30*, 1279–1291.
16. Robles, M.; Toscano, E.; Cotta, J.; et al. Antibiotic-induced liver toxicity: Mechanisms, clinical features and causality assessment. *Curr. Drug Saf.* **2010**, *5*, 212–222.
17. Montanari, E.; Bernardo, G.; Le Noci, V.; et al. Biofilm formation by the host microbiota: A protective shield against immunity and its implication in cancer. *Mol Cancer* **2025**, *24*, 148.
18. Mihai, M.M.; Holban, A.M.; Giurcaneanu, C.; et al. Microbial biofilms: Impact on the pathogenesis of periodontitis, cystic fibrosis, chronic wounds and medical device-related infections. *Curr. Top. Med. Chem.* **2015**, *15*, 1552–1576.
19. Martínez, J.L. Antibiotics and antibiotic resistance genes in natural environments. *Science* **2008**, *321*, 365–367.
20. Vasilev, K.; Cook, J.; Griesser, H.J. Antibacterial surfaces for biomedical devices. *Expert Rev. Med. Devices* **2009**, *6*, 553–567.
21. Vasilev, K.; Griesser, S.S.; Griesser, H.J. Antibacterial Surfaces and Coatings Produced by Plasma Techniques. *Plasma Process. Polym.* **2011**, *8*, 1010–1023.
22. Hasan, J.; Bright, R.; Hayles, A.; et al. Preventing Peri-implantitis: The Quest for a Next Generation of Titanium Dental Implants. *ACS Biomater. Sci. Eng.* **2022**, *8*, 4697–4737.
23. Bright, R.; Hayles, A.; Wood, J.; et al. Interplay between Immune and Bacterial Cells on a Biomimetic Nanostructured Surface: A "Race for the Surface" Study. *ACS Appl. Bio Mater.* **2023**, *6*, 3472–3483.
24. Romo-Rico, J.; Bright, R.; Krishna, S.M.; et al. Antimicrobial graphene-based coatings for biomedical implant applications. *Carbon Trends* **2023**, *12*, 100282.
25. Chernousova, S.; Epple, M. Silver as Antibacterial Agent: Ion, Nanoparticle, and Metal. *Angew. Chem. Int. Ed.* **2013**, *52*, 1636–1653.
26. Taheri, S.; Baier, G.; Majewski, P.; et al. Synthesis and antibacterial properties of a hybrid of silver–potato starch nanocapsules by miniemulsion/polyaddition polymerization. *J. Mater. Chem. B* **2014**, *2*, 1838–1845.
27. Alexander, J.W. History of the medical use of silver. *Surg. Infect.* **2009**, *10*, 289–292.
28. Beattie, M.; Taylor, J. Silver alloy vs. uncoated urinary catheters: A systematic review of the literature. *J. Clin. Nurs.* **2011**, *20*, 2098–2108.
29. Jiang, Y.; Zhang, Q.; Wang, H.; et al. Effectiveness of silver and iodine dressings on wound healing: A systematic review and meta-analysis. *BMJ Open* **2024**, *14*, e077902.
30. Liang, K.; Liu, Y.; Jiang, F. Analysis of therapeutic effect of silver-based dressings on chronic wound healing. *Int. Wound J.* **2024**, *21*, e70006.
31. Macgregor-Ramiasa, M.N.; Cavallaro, A.A.; Vasilev, K. Properties and reactivity of polyoxazoline plasma polymer films. *J. Mater. Chem. B* **2015**, *3*, 6327–6337.
32. Ramiasa, M.N.; Cavallaro, A.A.; Mierczynska, A.; et al. Plasma polymerised polyoxazoline thin films for biomedical applications. *Chem. Commun.* **2015**, *51*, 4279–4282.
33. Cavallaro, A.A.; Macgregor-Ramiasa, M.N.; Vasilev, K. Antibiofouling Properties of Plasma-Deposited Oxazoline-Based Thin Films. *ACS Appl. Mater. Interfaces* **2016**, *8*, 6354–6362.
34. Ninan, N.; Joseph, B.; Visalakshan, R.M.; et al. Plasma assisted design of biocompatible 3D printed PCL/silver nanoparticle scaffolds: In vitro and in vivo analyses. *Mater. Adv.* **2021**, *2*, 6620–6630.
35. Goreham, R.V.; Short, R.D.; Vasilev, K. Method for the Generation of Surface-Bound Nanoparticle Density Gradients. *J. Phys. Chem. C* **2011**, *115*, 3429–3433.
36. Hernandez-Lopez, J.L.; Bauer, R.E.; Chang, W.S.; et al. Functional polymers as nanoscopic building blocks. *Mater. Sci. Eng. C* **2003**, *23*, 267–274.

37. Macgregor-Ramiasa, M.; McNicholas, K.; Ostrikov, K.; et al. A platform for selective immuno-capture of cancer cells from urine. *Biosens. Bioelectron.* **2017**, *96*, 373–380.
38. Alemie, M.N.; Bright, R.; Nguyen, N.H.; et al. Surface Chemistry Induced IgG Unfolding and Modulation of Immune Responses. *ACS Appl. Mater. Interfaces* **2024**, *16*, 50507–50523.
39. Vasilev, K.; Sah, V.; Anselme, K.; et al. Tunable antibacterial coatings that support mammalian cell growth. *Nano Lett* **2010**, *10*, 202–207.
40. Nguyen, T.T.; Zhang, P.; Bi, J.; et al. Silver─Gallium Nano-Amalgamated Particles as a Novel, Biocompatible Solution for Antibacterial Coatings. *Adv. Funct. Mater.* **2024**, *34*, 2310539.
41. Haidari, H.; Kopecki, Z.; Bright, R.; et al. Ultrasmall AgNP-Impregnated Biocompatible Hydrogel with Highly Effective Biofilm Elimination Properties. *ACS Appl. Mater. Interfaces* **2020**, *12*, 41011–41025.
42. Vasilev, K.; Michelmore, A.; Martinek, P.; et al. Early Stages of Growth of Plasma Polymer Coatings Deposited from Nitrogen- and Oxygen-Containing Monomers. *Plasma Process. Polym.* **2010**, *7*, 824–835.
43. Taheri, S.; Cavallaro, A.; Christo, S.N.; et al. Substrate independent silver nanoparticle based antibacterial coatings. *Biomaterials* **2014**, *35*, 4601–4609.
44. Berger, A.; Edelsberg, J.; Oster, G.; et al. Patterns of Initial Antibiotic Therapy for Complicated Skin and Skin Structure Infections (cSSSI) in US Hospitals, 2000–2009. *Infect. Dis. Clin. Pract.* **2013**, *21*, 159–167.
45. O'Gara, J.P.; Humphreys, H. Staphylococcus epidermidis biofilms: Importance and implications. *J. Med. Microbiol.* **2001**, *50*, 582–587.
46. Otto, M. Staphylococcal Biofilms. *Microbiol. Spectr.* **2018**, *6*. https://doi.org/10.1128/microbiolspec.GPP3-0023-2018.
47. Pavlovsky, L.; Sturtevant, R.A.; Younger, J.G.; et al. Effects of temperature on the morphological, polymeric, and mechanical properties of Staphylococcus epidermidis bacterial biofilms. *Langmuir ACS J. Surf. Colloids* **2015**, *31*, 2036–2042.
48. Walker, J.T.; Jhutty, A.; Parks, S.; et al. Investigation of healthcare-acquired infections associated with Pseudomonas aeruginosa biofilms in taps in neonatal units in Northern Ireland. *J. Hosp. Infect.* **2014**, *86*, 16–23.
49. Le Feuvre, R.A.; Brough, D.; Iwakura, Y.; et al. Priming of Macrophages with Lipopolysaccharide Potentiates P2X7-mediated Cell Death via a Caspase-1-dependent Mechanism, Independently of Cytokine Production. *J. Biol. Chem.* **2002**, *277*, 3210–3218.
50. Park, B.S.; Lee, J.-O. Recognition of lipopolysaccharide pattern by TLR4 complexes. *Exp. Mol. Med.* **2013**, *45*, e66.
51. Mareddy, S.; Crawford, R.; Brooke, G.; et al. Clonal isolation and characterization of bone marrow stromal cells from patients with osteoarthritis. *Tissue Eng.* **2007**, *13*, 819–829.
52. Singh, S.; Jones, B.J.; Crawford, R.; et al. Characterization of a mesenchymal-like stem cell population from osteophyte tissue. *Stem Cells Dev.* **2008**, *17*, 245–254.
53. Chen, Z.; Klein, T.; Murray, R.Z.; et al. Osteoimmunomodulation for the development of advanced bone biomaterials. *Mater. Today* **2016**, *19*, 304–321.
54. He, W.; Elkhooly, T.A.; Liu, X.; et al. Silver nanoparticle based coatings enhance adipogenesis compared to osteogenesis in human mesenchymal stem cells through oxidative stress. *J. Mater. Chem. B* **2016**, *4*, 1466–1479.
55. Xiu, Z.; Zhang, Q.; Puppala, H.L.; et al. Negligible Particle-Specific Antibacterial Activity of Silver Nanoparticles. *Nano Lett.* **2012**, *12*, 4271–4275.
56. Liu, J.; Hurt, R.H. Ion Release Kinetics and Particle Persistence in Aqueous Nano-Silver Colloids. *Environ. Sci. Technol.* **2010**, *44*, 2169–2175.
57. Dreikausen, L.; Blender, B.; Trifunovic-Koenig, M.; et al. Analysis of microbial contamination during use and reprocessing of surgical instruments and sterile packaging systems. *PLoS ONE* **2023**, *18*, e0280595.
58. Wang, S.; van Dijl, J.M. Disinfection of medical devices with a steam machine that operates at atmospheric pressure and is suitable for home usage. *Sci. Rep.* **2025**, *15*, 25486.
59. Yang, H.; Wang, Y.; Yao, L.; et al. Antifouling Polymer Coatings for Bioactive Surfaces. *Langmuir : ACS J. Surf. Colloids* **2025**, *41*, 6471–6496.
60. Wang, A.; Pu, K.; Dong, B.; et al. Role of surface charge and oxidative stress in cytotoxicity and genotoxicity of graphene oxide towards human lung fibroblast cells. *J. Appl. Toxicol. JAT* **2013**, *33*, 1156–1164.
61. Werner, S.; Krieg, T.; Smola, H. Keratinocyte-fibroblast interactions in wound healing. *J. Investig. Dermatol.* **2007**, *127*, 998–1008.
62. Yang, A.; Cardona, D.L.; Barile, F.A. In vitro cytotoxicity testing with fluorescence-based assays in cultured human lung and dermal cells. *Cell Biol. Toxicol.* **2002**, *18*, 97–108.
63. Ninan, N.; Muthiah, M.; Park, I.-K.; et al. Faujasites Incorporated Tissue Engineering Scaffolds for Wound Healing: In Vitro and In Vivo Analysis. *ACS Appl. Mater. Interfaces* **2013**, *5*, 11194–11206.
64. Wiegand, C.; Hipler, U.C. Evaluation of biocompatibility and cytotoxicity using keratinocyte and fibroblast cultures. *Ski. Pharmacol Physiol* **2009**, *22*, 74–82.

65. Mayol, L.; De Stefano, D.; De Falco, F.; et al. Effect of hyaluronic acid on the thermogelation and biocompatibility of its blends with methyl cellulose. *Carbohydr. Polym.* **2014**, *112*, 480–485.
66. Burrell, R.E. A scientific perspective on the use of topical silver preparations. *Ostomy/Wound Manag.* **2003**, *49*, 19–24.
67. Nadworny, P.L.; Wang, J.; Tredget, E.E.; et al. Anti-inflammatory activity of nanocrystalline silver in a porcine contact dermatitis model. *Nanomed. Nanotechnol. Biol. Med.* **2008**, *4*, 241–251.
68. Warriner, R.; Burrell, R. Infection and the chronic wound: A focus on silver. *Adv. Ski. Wound Care* **2005**, *18*, 2–12.
69. Xie, H.; Pei, W.; and Wu, J. Effect of exposure of osteoblast-like cells to low-dose silver nanoparticles: Uptake, retention and osteogenic activity. *Artif. Cells Nanomed. Biotechnol.* **2019**, *47*, 260–267.
70. Xiao, K.; Liu, C.; Tu, Z.; et al. Activation of the NF-κB and MAPK Signaling Pathways Contributes to the Inflammatory Responses, but Not Cell Injury, in IPEC-1 Cells Challenged with Hydrogen Peroxide. *Oxidative Med. Cell. Longevity* **2020**, *2020*, 5803639.
71. Chen, J.; Chen, X.; Xuan, Y.; et al. Surface functionalization-dependent inflammatory potential of polystyrene nanoplastics through the activation of MAPK/NF-κB signaling pathways in macrophage Raw 264.7. *Ecotoxicol. Environ. Saf.* **2023**, *251*, 114520.
72. Arya, P.N.; Saranya, I.; Selvamurugan, N. Crosstalk between Wnt and bone morphogenetic protein signaling during osteogenic differentiation. *World J Stem Cells* **2024**, *16*, 102–113.
73. Wang, L.; Ruan, M.; Bu, Q.; et al. Signaling Pathways Driving MSC Osteogenesis: Mechanisms, Regulation, and Translational Applications. *Int. J. Mol. Sci.* **2025**, *26*, 1311.
74. Bright, R.; Visalakshan, R.M.; Simon, J.; et al. Manipulation of Serum Protein Adsorption by Nanoengineered Biomaterials Influences Subsequent Immune Responses. *ACS Biomater. Sci. Eng.* **2024**, *10*, 6230–6240.
75. Sharifianjazi, F.; Sharifianjazi, M.; Irandoost, M.; et al. Advances in Zinc-Containing Bioactive Glasses: A Comprehensive Review. *J Funct Biomater* **2024**, *15*, 258.
76. Elbasuney, S.; El-Sayyad, G.S.; Radwan, S.M.; et al. Antimicrobial, and Antibiofilm Activities of Silver Doped Hydroxyapatite: A Novel Bioceramic Material for Dental Filling. *J. Inorg. Organomet. Polym. Mater.* **2022**, *32*, 4559–4575.
77. Marsico, M.; Azari, R.; Curcio, M.; et al. Enhancing the Antibacterial Properties of Chitosan Coatings: Ag@Chitosan and Chitosan from Insects. *Coatings* **2024**, *14*, 925.